

Structural Characteristics and *In Vitro* Biodegradation of a Novel Zn-Li Alloy Prepared by Induction Melting and Hot Rolling



SHAN ZHAO, CAMERON T. MCNAMARA, PATRICK K. BOWEN,
NICHOLAS VERHUN, JACOB P. BRAYKOVICH, JEREMY GOLDMAN,
and JAROSLAW W. DRELICH

Zinc shows great promise as a bioabsorbable metal; however, the low tensile strength of pure zinc limits its application for endovascular stent purposes. In this study, a new Zn- x Li alloy (with $x = 2, 4, 6$ at. pct) was prepared by induction melting in an argon atmosphere and processed through hot rolling. Structures of the formulated binary alloys were characterized by X-ray diffraction and optical microscopy. Mechanical testing showed that the incorporation of Li into Zn increased ultimate tensile strength from <120 MPa (pure Zn) to >560 MPa ($x = 6$ at. pct). *In vitro* corrosion behavior was evaluated by immersion tests in simulated body fluid. The Zn-2Li and Zn-4Li corrosion study demonstrated that corrosion rates and products resemble those observed for pure Zn *in vivo*, and in addition, the Zn-4Li alloy exhibits higher resistance to corrosion as compared to Zn-2Li. The findings herein encourage further exploration of Zn-Li systems for structural use in biomedical vascular support applications with the ultimate goal of simplifying stent procedures, thereby reducing stent-related complications.

DOI: 10.1007/s11661-016-3901-0

© The Minerals, Metals & Materials Society and ASM International 2016

I. INTRODUCTION

BIOABSORBABLE stents are envisaged to support the arterial wall during remodeling after stent deployment and to degrade harmlessly thereafter. This new generation of endovascular stents may eliminate the potential for chronic inflammation^[1] and thrombosis risks^[2] of permanent stents. They could also alleviate the repetition of invasive procedures when stenting at the same site in the event of restenosis.^[3] Over the past decade, polymeric and metallic materials have been widely investigated for endovascular stent applications with very limited success.^[4–7] The previous reports demonstrated that neither polymers nor metallic candidates such as iron and magnesium are ideal for biodegradable stenting applications due to either poor mechanical properties,^[7–10] incomplete bioabsorption of corrosion products,^[11] or premature degradation.^[12] Consequently, the search for new bioabsorbable materials continues.^[7]

Zinc is one of the most abundant nutritionally essential elements in the human body^[13] and studies have been initiated examining zinc as a bioabsorbable material in recent years.^[14] One major concern regarding

the use of a pure zinc stent is the material's low intrinsic ultimate tensile strength (UTS) of about 120 MPa or less, where the cardiovascular stent application requires a material with UTS closer to 300 MPa.^[15] Improvements in mechanical properties of zinc can be approached through alloying^[16,17] and manipulation of metal micro/nanostructure.^[18,19] Lithium is one of the few elements with significant solubility in zinc, and Zn-Li is therefore among a few potentially age-hardenable systems.

Hypoeutectic 2 at. pct Li (0.2 wt pct), eutectic 4 at. pct Li (0.4 wt pct), and hypereutectic 6 at. pct Li (0.7 wt pct) compositions were chosen for this study based on the phase diagram produced by Pelton^[20] (Figure 1). The eutectic reaction under the casting conditions used herein is expected to result in prolific lamellar formation during cooling, so that much of the available Li is consumed and the only Li available for post-solidification strengthening is what is left in supersaturation upon cooling below the eutectic temperature in (Zn)Li regions. Therefore, precipitation hardening is expected to play a major role in the 2 pct, a minor role in the 4 pct, and a negligible role in the 6 pct alloy. However, the LiZn_4 formed as part of the lamellar structure does have an impact on yield and ultimate strength as the shear moduli between this and the Zn(Li) phase is different, and the strength increment is proportional to $1/\lambda^{1/2}$, where λ is the lamellar spacing, according to a Hall-Petch relation. This effect is expected to play a major role in the 6 pct alloy, a minor role in the 4 pct, and a negligible role in the 2 pct alloy. Strengthening from further grain size refinement is also possible since the recrystallization from hot rolling may produce a

SHAN ZHAO, CAMERON T. MCNAMARA, PATRICK K. BOWEN, NICHOLAS VERHUN, JACOB P. BRAYKOVICH and JAROSLAW W. DRELICH are with the Department of Materials Science and Engineering, Michigan Technological University, Houghton, MI 49931. Contact e-mail: jwdrelic@mtu.edu JEREMY GOLDMAN is with the Department of Biomedical Engineering, Michigan Technological University, Houghton, MI 49931.

Manuscript submitted June 23, 2016.

Article published online January 3, 2017

finer structure than the as-cast material in all the three alloys, although grain size is not explicitly measured here. Work hardening is not anticipated to play a role in these tensile or hardness tests as the alloys here are annealed directly following the hot rolling process, which is intended to reduce stored dislocation energy while precipitating as much LiZn_4 as possible. If crystalline slip becomes too difficult because of the aforementioned obstacles to dislocation motion during loading of an HCP crystal, deformation *via* twinning mechanisms may be activated which allow deformation through much larger scale atomic rearrangements.

An endovascular metallic stent weighs approximately 50 mg.^[14] If it degrades completely within one year, the expected daily dose of Zn and Li would be below 140 and 1 μg , respectively, for an alloy containing 14 at. pct Li (Table I). These values are roughly two orders of magnitude below the daily bodily consumption allowances^[21,22] and thus the toxic potential of a zinc-lithium stent is anticipated to be negligible in terms of the overall quantities of the elements released. With regard to local toxic effects, rapid transport of ions in vascular tissue^[23] would prevent elemental enrichment and cytotoxicity in the implant's vicinity.^[15] Lithium has been successfully used in bioabsorbable Mg alloy LAE442

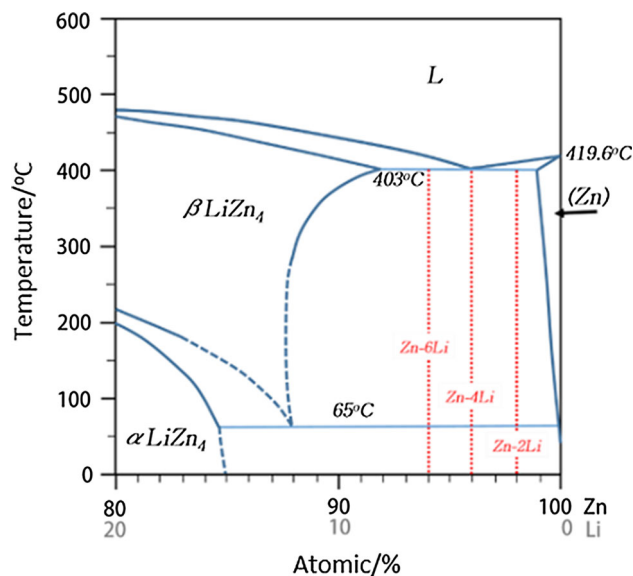


Fig. 1—Zinc-lithium phase diagram (prepared based on Ref. [20]).

Table I. Estimated Daily Release of Zn and Li from a 50 mg Stent Compared to Daily Bodily Consumption Allowances

Intake	Daily Allowance for Adult males	Estimated Release from Zn-Li Alloy*
Zn	10 mg ^[21]	140 μg
Li	0.6 mg ^[20]	1 μg

*The daily amount of release can be obtained by dividing the mass of Zn and Li assuming a full degradation timeframe of 365 days. For an alloy of Zn-14 at. pct Li and a stent mass of 50 mg, the total mass of Li is 0.38 mg so the daily release of Li into biological system is 1 μg .

which has 4 wt pct of lithium, 4 wt pct of aluminum, and 2 wt pct of rare-earth elements. LAE442 has been shown to be non-allergenic,^[24] biodegradable, and to degrade more slowly than pure magnesium without the formation of radiographically observable gas^[25,26] and with a more uniform degradation behavior.^[26] It has been considered as the most promising implant material for orthopedic use.^[27]

Based on this evidence, alloying zinc with lithium is expected to produce a stent material with favorable biocompatibility and reasonable strength. To our knowledge, no systematic research has been reported on the Zn-Li alloy as a biodegradable implant material. Most of the existing studies in the binary Li-Zn system focus on thermodynamic properties,^[20] the crystal structures of LiZn_x compounds,^[28] preliminary charge-discharge characteristics,^[29] and the reactivity of lithium-ion batteries.^[30] In the rechargeable Li-ion battery area, the Li-Zn alloys have been considered as an alternative to graphite-based anode materials.^[28] As for the five binary Li-Zn intermetallic phases, LiZn was considered to be crystallized in the NaTi structure type,^[31] and LiZn_4 was proposed to have a Mg-type structure with a random distribution of Li and Zn.^[32] Crystal structures of Li_2Zn_3 at low- and high-temperature modifications were determined by single-crystal X-ray diffraction techniques in 2012.^[33] The structures of Li_2Zn_5 and LiZn_2 phases remain unexplored.

This new series of biodegradable Zn-Li alloys is formulated, cast, and processed through hot rolling in this study to simulate commercial processes such as extrusion. The alloys are characterized regarding their as-processed tensile properties and degradation in simulated body fluid.

II. MATERIALS AND METHODS

A. Alloy Preparation

Pure Zn (99.99 wt pct, Alfa Aesar company, Ward Hill, MA) and pure Li foil (99.9 wt pct, Alfa Aesar company, Ward Hill, MA) were loaded into a graphite crucible in an inert atmosphere glove box to avoid atmospheric oxidation of lithium. A custom vacuum induction melting setup at Michigan Tech (Figure 2(a) through (c)) was used to fabricate the Zn-Li alloys. They were cast by induction melting with a power of ~3 kW under a 0.9 atm argon atmosphere. The ultimate vacuum level was 2×10^{-4} torr. A stepper motor controlled by a custom LabView (National Instruments, Austin, TX) script tilt-poured the melt into a 50-mm-diameter stainless steel mold. These ingots were squared and sectioned to a size of $35 \times 35 \times 60$ mm and underwent deformation processing *via* hot rolling to simulate the extrusion process used in conventional stent tube forming. Before rolling, alloys were placed in a box furnace at 662 °F (350 °C) for several minutes until reaching the furnace temperature. The rolling process was performed on a Fenn (Newington, CT) 2-high mill equipped with 133 mm rolls at 42 rpm (Figure 2(d)). After three passes through the rolling mill, the sample

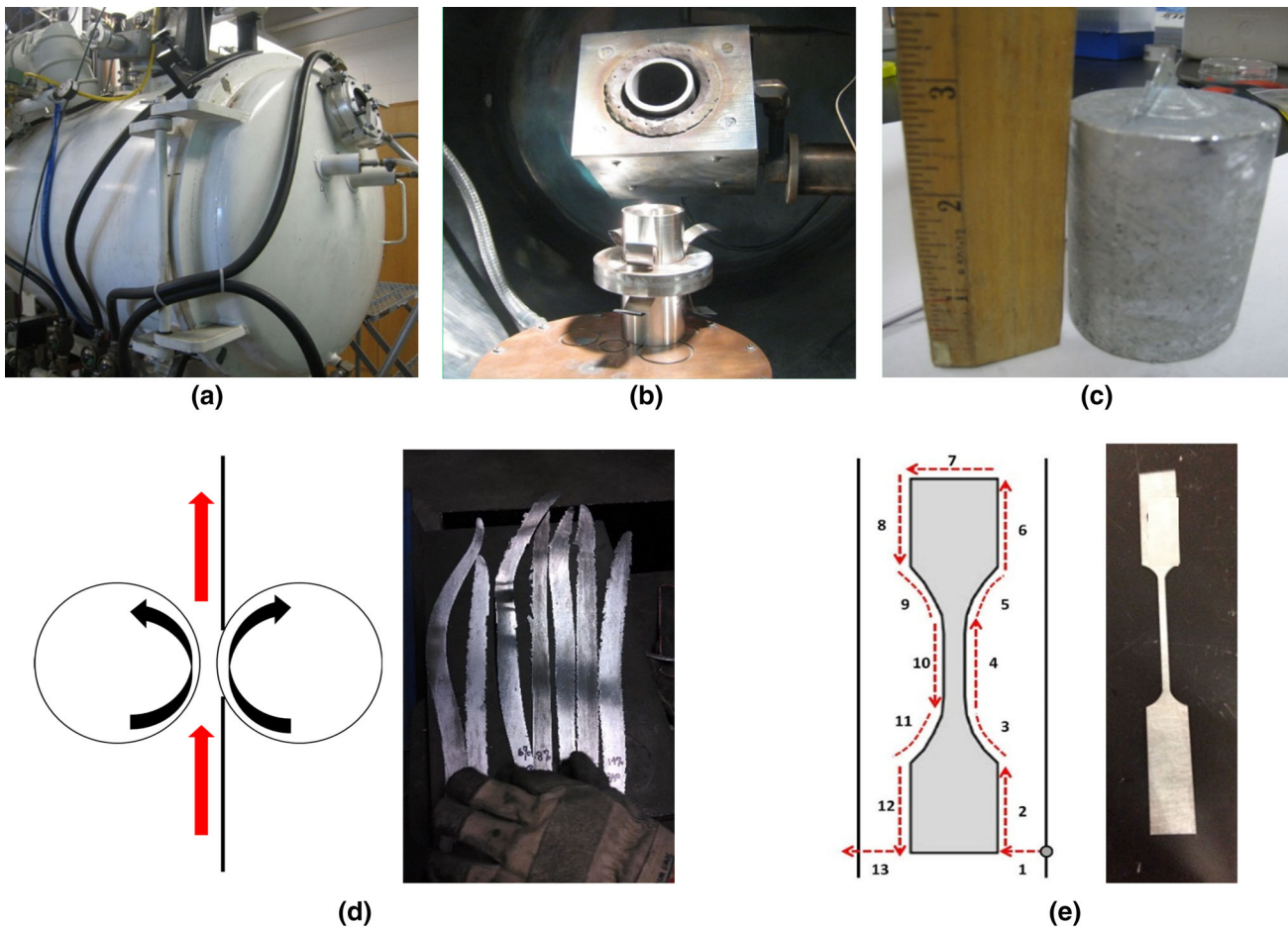


Fig. 2—Fabrication of Zn-Li ingots, strips, and dogbone tensile bars; (a) through (c) vacuum induction melting setup for alloy ingots; (d) uniaxial rolling process to reduce ingots from 1.8 mm to $\sim 300 \mu\text{m}$; (e) layout of Japax wire EDM g-code for precision cutting of dogbone tensile bars.

thickness was recorded and the sample was returned to the furnace for 3 minutes. The final sheet was reduced from 35 mm to approximately $300 \mu\text{m}$ in thickness for a total reduction of cross-sectional area of 99 pct. From these sheets, dogbone tensile bars were cut for standard tests per ASTM E8/E8M-11 using wire electro discharge machining (wire EDM) on a PC-controlled Japax Lux-3 (McWilliams EDM, Brighton, MI) (Figure 2(e)).

B. Alloy Characterization

Inductively Coupled Plasma Optical Emission Spectrometry (ICP-OES) (PerkinElmer Optima 7000DV, Waltham, MA) was utilized in detecting the compositions of Zn alloy sheets after hot rolling. To produce a solution suitable for ICP-OES analysis, 250 mg of each alloy was dissolved in 40 mL of 6M HCl, which was diluted for analysis.

Microscopy samples of both as-cast and hot-rolled material were mounted in epoxy and polished with 600-grit, 800-grit, and 1200-grit silicon carbide. Final polishing steps were performed using 6, 1, and $0.1 \mu\text{m}$ diamond cloth and $0.05 \mu\text{m}$ alumina slurry on micro-fiber. Microstructure of alloys was recorded using a Leica EC3 (Leica Microsystems; Buffalo Grove, Illinois)

digital camera on an Olympus PMG-3 metallograph (Olympus, Shinjuku, Tokyo).

X-ray diffraction (XRD) was performed on an XDS2000 θ/θ X-ray diffractometer (Scintag Inc., Cupertino, CA) with $\text{CuK}\alpha$ radiation ($k = 1.540562 \text{ \AA}$). The scans were performed continuously from 20 deg to 100 deg in 2θ at a speed of 0.6 deg/min with a step size of 0.02 deg.

Uniaxial tensile tests were performed using an Instron 5984 electro-mechanical testing machine equipped with a 150 kN load cell (Instron, Norwood, MA). All tests were performed at an initial strain rate of 10^{-3} s^{-1} .

Vickers microhardness (HV) was measured using an M-400-G1 digital hardness tester (LECO, St Joseph, MI) at a load of 200 g for 5 seconds and a minimum of 10 indentations per sample.

Electrochemical measurements were made with a PARSTAT 4000, teamed with the Versa Studio software package (AMETEK/Princeton Applied Research, Berwin, PA). The PARSTAT 4000 is a potentiostat/galvanostat combined with a frequency response analyzer (FRA) contained in a single unit. A three-electrode setup was employed: the working electrode (Zn-Li coupons, immersed area of 1 cm^2) with Ag/AgCl (SSE) and graphite as the reference and counter

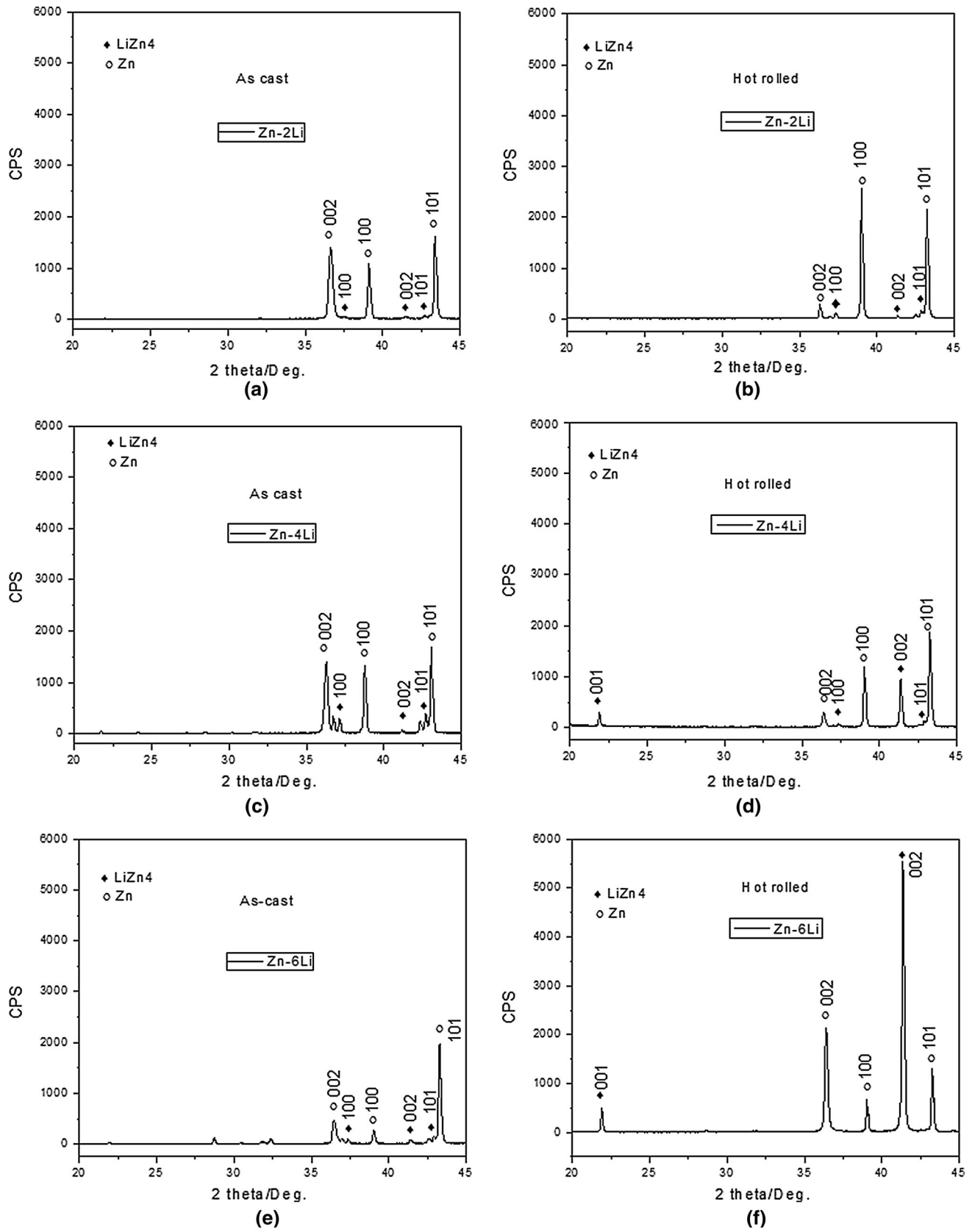


Fig. 3—XRD patterns of the as-cast and hot-rolled alloys with different compositions: (a) as-cast Zn-2Li, (b) hot-rolled Zn-2Li, (c) as-cast Zn-4Li, (d) hot-rolled Zn-4Li, (e) as-cast Zn-6Li, and (f) hot-rolled Zn-6Li.

electrodes, respectively. The test medium was simulated body fluid in a 98.6 °F (37 °C) incubator with 5 pct CO₂ supply, the composition of which is discussed below and also shown in Table II.

C. *In vitro* Immersion Test and Characterization of Corrosion Product

In vitro corrosion tests were carried out in modified simulated body fluid (SBF). In contrast with the classic tris-buffered (trishydroxymethyl-aminomethane) SBF solution, the content of bicarbonate was elevated to the level found in blood plasma; conveniently, the buffering function of tris was accomplished by the additional bicarbonate. The adoption of this bicarbonate buffering system was important, as it resembles the *in vivo* environment of the acid–base homeostasis of a living host, including the human body. Ion concentrations of the modified SBF used here, traditional SBF,^[34] and human blood plasma are listed in Table II.

The rolled alloy sheets of 300 μm thickness were cut into 1 × 1 cm². Pure Zn was also used as control. *In vitro* submersion took place in 50 mL centrifuge tubes, where the coupons were covered with 40 mL of SBF medium and placed in an incubator at 98.6 °F (37 °C) and 5 pct CO₂ atmosphere for 4, 7, and 14 days. The ratio of solution volume to specimen area (V/S) was ~20 ml/cm², which was suggested by the ASTM G31-72 to ensure the volume is large enough to avoid medium changes during corrosion.^[35] The pH was measured at 7.2 to 7.4 throughout the experiment.

Although ISO 10993-15:2000 recommended a V/S ratio of less than 1 mL/cm², various V/S ratios ranging from 0.33 mL/cm²^[36] to 7375 mL/cm²^[37] have been chosen by researchers. It is difficult to specify a standard V/S for all immersion tests since the ratio should be

Table II. Ion Concentrations of Human Blood Plasma and the Experimental Simulated Body Fluid (SBF)

Ion	Blood Plasma	Simulated Body Fluid ^[34]	Revised Simulated Body Fluid
Na ⁺	142.0	142.0	160.0
K ⁺	5.0	5.0	4.0
Mg ²⁺	1.5	1.5	1.0
Ca ²⁺	2.5	2.5	2.5
Cl ⁻	103.0	148.8	142.0
HCO ₃ ⁻	27.0	4.2	26.0
HPO ₄ ²⁻	1.0	1.0	1.0
SO ₄ ²⁻	0.5	0.5	0.5
pH	7.2 to 7.4	7.4	7.4

based on the implantation environment the researchers intend to mimic.^[38] Therefore, even for the same alloy from different research groups, the *in vitro* corrosion results are not compared.^[38] It is known that *in vitro* methods are quick and relatively inexpensive, but it is also apparent that predicting *in vivo* behavior from *in vitro* testing can be misleading.^[37] Local pH, impurities, processing, the concentration of the pitting anion,^[39] and proteins^[40] can all play a role in metallic corrosion.

Surface morphological and elemental analyses were carried out on the samples following *in vitro* corrosion using a JSM 6400 scanning electron microscope (SEM) (JEOL, Peabody, MA) equipped with an energy-dispersive spectrometer (EDS). The accelerating voltage and working distance used for all samples were 20 kV and 39 mm, respectively. Fourier Transform Infrared Spectroscopy (FTIR) was conducted in diffuse reflectance mode with a Genesis II FTIR spectrophotometer (SUNY Genesso, Genesso, NY). A series of 1024 scans was performed at 1 cm⁻¹ resolution ranging from 400 to 4000 cm⁻¹.

III. RESULTS AND DISCUSSION

A. Elemental Analysis

Experimental compositions of the alloys are listed in Table III. For all three Zn-Li alloys, the experimental compositions from ICP-OES were slightly lower than the nominal compositions. Ni and Fe were detected as trace impurities from Zn; Ni remained below the detection limit for the three alloys and Fe concentration was also very low.

B. XRD Analysis

XRD patterns for Zn-*x*Li (*x* = 2, 4, 6 at. pct) before and after hot rolling are shown in Figure 3. All the investigated samples exhibit dual-phasic character with the main phase of zinc and minor phase of LiZn₄. Patterns were collected at room temperature, and the LiZn₄ phase present in all the as-cast and as-processed materials is assumed to be of the low-temperature α-variety as all cooling was done slowly in air to allow the eutectoid relaxation to occur. For the as-cast samples, peaks corresponding to Zn are high and narrow, indicating relatively large grain sizes and very little lattice deformation. Peaks corresponding to the intermetallic phase LiZn₄ in the as-cast samples have the highest relative intensities in the Zn-4Li alloy with peaks

Table III. ICP-OES Compositional Analysis of Rolled Zn Alloys

Sample ID	Li (at. pct) Nominal	Li (at. pct) Experimental	Fe (at. pct)	Ni (at. pct)	Zn (at. pct)
Zn	<0.01	<0.01	<0.01	<0.10	bal.
Zn-2Li	2.00	1.10	0.03	<0.10	bal.
Zn-4 Li	4.00	3.20	0.01	<0.10	bal.
Zn-6 Li	6.00	5.50	0.01	<0.10	bal.

from sets of (101), (002), and (100) planes, indicating prolific nucleation and growth of LiZn₄ during solidification at this composition.

After hot rolling, the rolling direction–transverse direction (RD–TD) cross sections were examined, and the preferential orientations of LiZn₄ and the Zn lattice changed as observed by the increased intensities of the (002) and (001) peaks relative to the (101) peak for the same phase in both cases (Figure 3). Peaks corresponding to LiZn₄ also increased in intensity relative to those for the Zn lattice, with the increase of Li due to larger volume fractions of LiZn₄ available in the more concentrated alloys (Figure 4). Minor peaks at 2θ = 21.7 and 89.9 deg are observed which do not correspond to known reflections in the JCPDS-ICDD database. In order to determine if these peaks originate from the Zn + LiZn₄ mixture, an estimation of the structure factor (F) using these two phases was carried out using Eq. [1] through [3] with results displayed in Table IV.

(1) If disordered (*i.e.*, solid solution):

$$F = 2 \times f_{\text{ave}} \left[e^{i2\pi(\frac{1}{3}h + \frac{2}{3}k + \frac{1}{4}l)} + e^{i2\pi(\frac{2}{3}h + \frac{1}{3}k + \frac{3}{4}l)} \right] \quad [1]$$

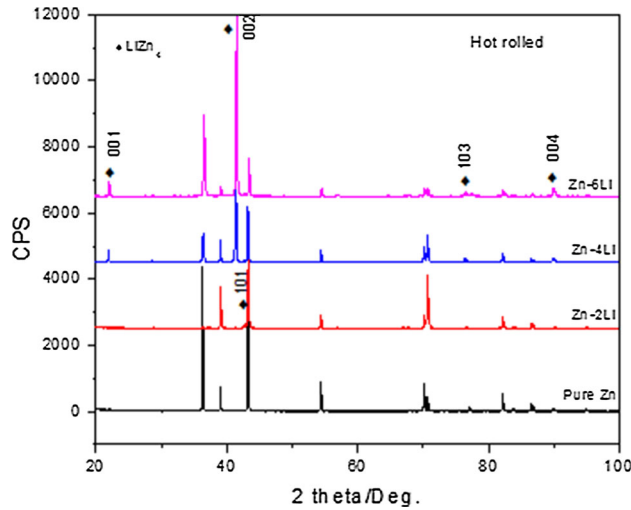


Fig. 4—Full-scan range XRD patterns of hot-rolled alloys with different compositions. LiZn₄ peaks are identified.

Table IV. Structure Factors for Ordered and Disordered States of Zn(Li) + LiZn₄

<i>h</i>	<i>k</i>	<i>l</i>	2θ	Sin/λ	<i>F</i> _{Li}	<i>F</i> _{Zn}	<i>F</i> ² (disordered)	<i>F</i> ² (ordered)
0	0	1	22	0.24	1.65	20.5	0	1076
0	0	2	42	0.43	1.20	15.5	2556	615
0	0	3	64	0.58	0.82	12.5	0	399
0	0	4	89	0.65	0.70	11.5	1396	349
1	0	1	43	0.44	1.15	15.0	448	571
1	0	0	37	0.39	1.30	15.8	166	639

$$f_{\text{ave}} = \frac{4}{5} \times f_{\text{Zn}} + \frac{1}{5} \times f_{\text{Li}} \quad [2]$$

(2) If ordered (*i.e.*, dual-phasic):

$$F = 2 \times \frac{1}{5} f_{\text{Li}} e^{i2\pi(\frac{1}{3}h + \frac{2}{3}k + \frac{1}{4}l)} + 2 \times \frac{4}{5} f_{\text{Zn}} e^{i2\pi(\frac{2}{3}h + \frac{1}{3}k + \frac{3}{4}l)} \quad [3]$$

The theoretical values of 2θ at (00*l*) planes (Table V) are then obtained from

$$\sin^2 \theta = \frac{\lambda^2}{4a^2} \left(h^2 + k^2 + l^2 \frac{a^2}{c^2} \right), \quad [4]$$

where LiZn₄ has the structure *P6*₃/*mmc* (no. 194, HCP) with *a* = 0.27702(8) and *c* = 0.43785(9) nm.

The matching of the theoretical 2θ values from structure factor calculations with experimentally observed diffraction peaks indicates that the two unidentified peaks do originate from the Zn + LiZn₄ structure but are not tabulated in the current database. In a previous study on α-LiZn₄ powder,^[41] a structural model was determined in which both Zn and Li were seated in the (1/3, 2/3, 1/4) 2*c* site with a Li/Zn ratio equal to 0.28 (experimental value). This phase is isostructural with elemental HCP Zn, consistent with the findings of the current study. It is concluded that hot rolling promotes precipitation of the ordered LiZn₄ phase and produces texture in which the matrix and the LiZn₄ phase both have preferred orientations with the *c*-axis normal to the RD–TD plane. Interestingly, no occurrence of the (003) reflection was observed in Reference 28 or the present study, though this is an allowable reflection based on the structure factor equations above for the dual-phasic approximation. This could suggest a different arrangement of Zn and Li atoms in the LiZn₄ phase, or the peak intensity could simply be below the resolution limit of the XRD and filtered out of the spectrum.

C. Microstructural Features

Optical micrographs from RD–TD cross sections of alloy sheets before and after hot rolling are shown in Figure 5. Microstructures are consistent with Scheil/Scheil-Gulliver non-equilibrium solidification

conditions. For Zn-2Li, small amounts of Zn + LiZn₄ are present in the α -Zn matrix. With Zn-4Li, a mixture of lamellar Zn + LiZn₄ grains and α -Zn grains is observed. The lamellae are observed in grains with apparently random orientation. For Zn-6Li, dendritic arms and trunks are observed consisting of Zn + LiZn₄ which have a very tight lamellar spacing with interdendritic channels of Zn(Li). The random arrangement of grains observed in the hypoeutectic alloy tended toward directional solidification with increasing Li content. The fact that pro-eutectic grains of α -Zn are observed for Zn-4 at. pct Li in Figure 5 points to a slightly lower experimental composition than 4 at. pct Li in this cross section. This is confirmed by ICP-OES results, as shown in Table III.

After the hot rolling and annealing process, the Zn-4Li and Zn-6Li samples exhibit severe rolling texture and no occurrence of equiaxed grains exists; dendrite arms and trunks are refined and the grain width decreases from ~ 50 to ~ 10 μm . In contrast, the hypoeutectic alloy exhibits equiaxed grains almost exclusively. This observation points to dynamic recrystallization occurring during the hot rolling process or after static recrystallization for this alloy but not for the higher Li alloys. However, the texture that develops during rolling is retained: the XRD scans in Figure 3 show an increase

in the intensity of the (100) peak relative to the (101) for all the three alloys.

For all the alloys, the high-temperature intermetallic phase β -LiZn₄, present in both lamellar structures and the as-precipitated particles relaxes to the room-temperature α -LiZn₄ phase at the eutectoid temperature of 338 K (65 °C).^[20] Evidence of this reaction was not observed metallographically, and it is assumed that all β -LiZn₄ converts to α -LiZn₄ with ease.

D. Mechanical Testing

Yield strength, UTS, and ductility values for all tested alloys are shown in Figure 6. The 300 MPa UTS and 200 MPa yield strength benchmarks for bioabsorbable stent materials^[14] are exceeded at all alloying levels. Higher contents of Li yield higher tensile strengths due to the larger volume fractions of the LiZn₄ phase. Ductilities of the Zn-2Li and Zn-4Li alloys are favorable compared to very limited ductility of Zn-6Li in view of benchmark values of 15-18 pct elongation to failure for bioabsorbable stent materials.^[14] While these are excellent properties for a stent material, further study is needed to delineate the exact strengthening mechanisms operating in each alloy. Based on these empirical strength and ductility values, alloys with lower content of Li (2 and 4 at. pct, nominally) were selected for *in vitro* corrosion testing.

As shown in Figure 7, the hardness of Zn-2Li increases from 85 ± 6 to 98 ± 6 after hot rolling, and Zn-4Li and Zn-6Li increase from 98 ± 6 to 115 ± 6 and 115 ± 8 to 136 ± 9 , respectively. This is a 15 pct percent increase in hardness for Zn-2Li and 18 pct for Zn-6 at. pct. This can be attributed to precipitation strengthening through the formation of LiZn₄, evidenced by XRD, and boundary strengthening by the highly refined grain

Table V. Theoretical and Experimental Values of 2θ for $h = k = 0$ and $l = 1, 2, 3$, or 4

(hkl)	2θ (Theoretical)	2θ (Experimental)
001	21.80	21.70
002	41.46	41.40
003	63.71	×
004	89.94	89.95

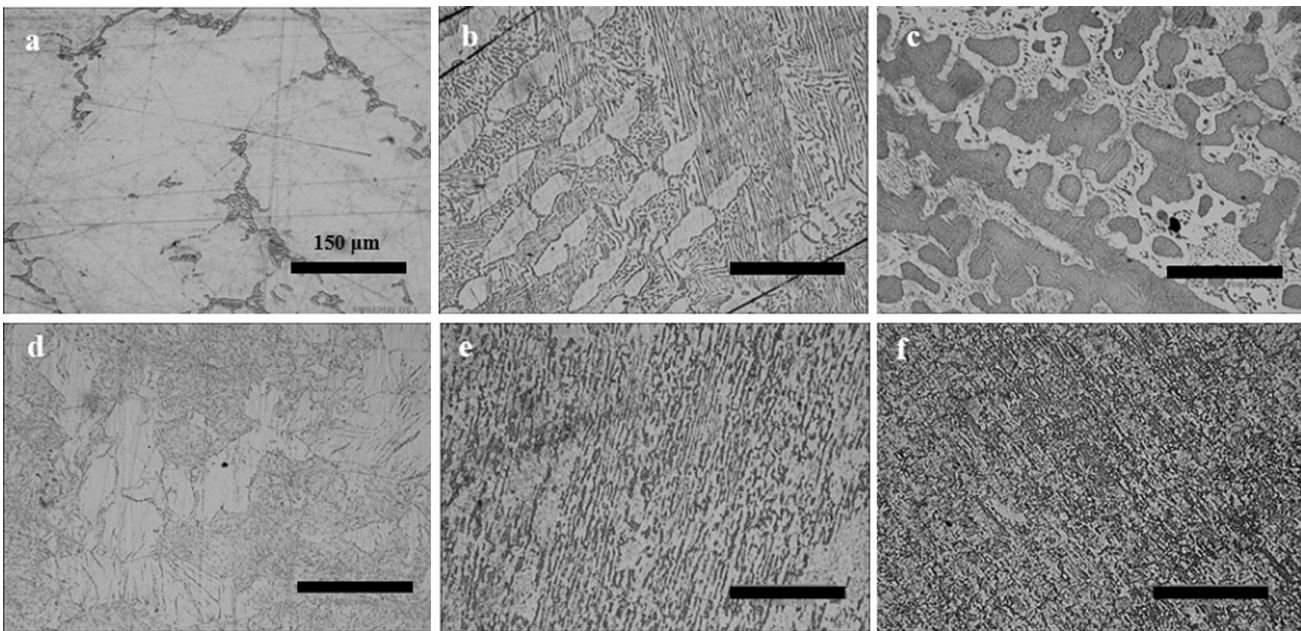


Fig. 5—Optical micrographs of the as-cast (a) through (c) and hot-rolled (d) through (f) Zn-Li alloys with Li content increasing from 2 to 4 to 6 at. pct from left to right. The scale bar in panel a applies to all six micrographs.

structure (Figure 5). Zn-6 at. pct has the finest grains (only a few microns in width) and the highest volume fraction of LiZn₄; this combination gives the highest hardness, and the strengthening effect from hot rolling is more evident. An increase in dislocation density is highly probably following a 99 pct reduction in area, but much of the hardening effect is likely lost during the post-deformation recovery anneal. Texture effects might also play a role in this system as some preferential orientation of LiZn₄ is detected in Figure 3, which may lead to anisotropy in mechanical properties as a consequence of the limited number of slip systems available in Zn.

E. Corrosion Rate in SBF

For the investigated Zn-Li alloys and pure Zn, the approximate values of corrosion potential and corrosion current were determined from Tafel slopes.^[42] In order

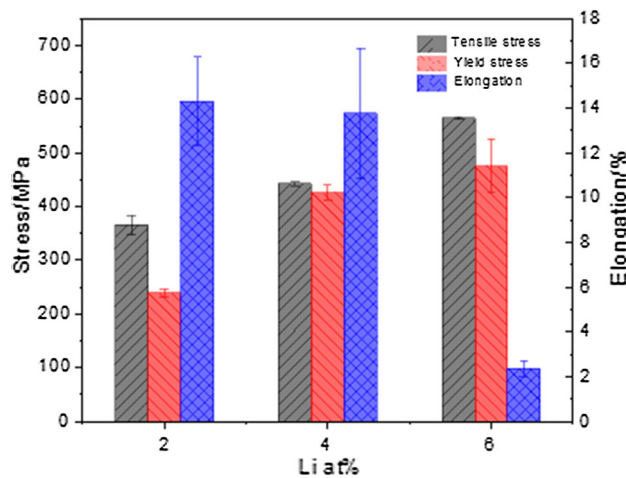


Fig. 6—Ultimate tensile strength (UTS), yield strength, and elongation to failure of Zn-2Li, Zn-4Li, and Zn-6Li with error bars representing standard deviation in measurement.

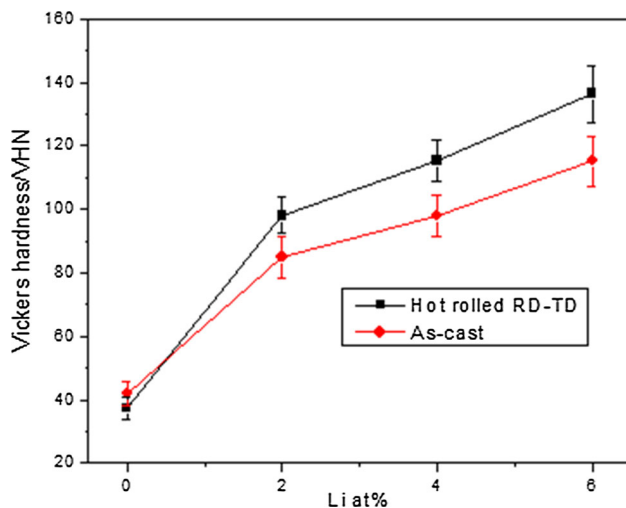


Fig. 7—Vickers microhardness of hot-rolled and the as-cast alloys with different compositions.

to estimate the corrosion current values, the anodic curve was extrapolated until it intersected with the level of corrosion potentials as shown in Figure 8 and Table VI. A high current density (current on the surface) at the corresponding potential indicates a high corrosion rate of the alloy. Comparison between the Zn-Li alloy curves with pure Zn shows that the alloys with 2 and 4 at. pct Li have similar curves. The corrosion rates of the various tested materials are estimated (Table VI, column 3) through Tafel extrapolation.

The Zn-4 at. pct Li alloy exhibits the lowest current density (3.80 $\mu\text{A}/\text{cm}^2$) and therefore the highest resistance to corrosion compared to the other two samples. The corrosion resistance could be due to the formation of a protective passive layer, typically the surface-product surface film (Figure 8). The thicker the passive layer and better attachment to the surface, the higher the corrosion resistance of the alloy.

Corrosion rates were estimated in terms of penetration rate (CR) using the Faraday's law as follows:

$$CR = K_1 \frac{i_{\text{corr}}}{\rho} EW \quad [5]$$

$$EW = \frac{1}{\sum \frac{n_i f_i}{w_i}}, \quad [6]$$

where CR is in mm/year, i_{corr} in $\mu\text{A}/\text{cm}^2$, $K_1 = 3.27 \times 10^{-3}$ mm g/ μA cm year, ρ is the density in g/cm³, EW is the equivalent weight of the alloy, f_i is the mass fraction of the i th element in the alloy, w_i is the atomic weight of the i th element in the alloy, and n_i is the valence of the i th element of the alloy.

According to the calculation results summarized in Table VI, penetration rates for Zn-Li alloys in SBF are 0.05 to 0.06 mm year⁻¹, and are comparable to Zn studied in plasma (0.1 mm year⁻¹),^[35] whole blood (0.05 mm year⁻¹),^[35] and *in vivo* (0.02 to 0.05 mm year⁻¹).^[15]

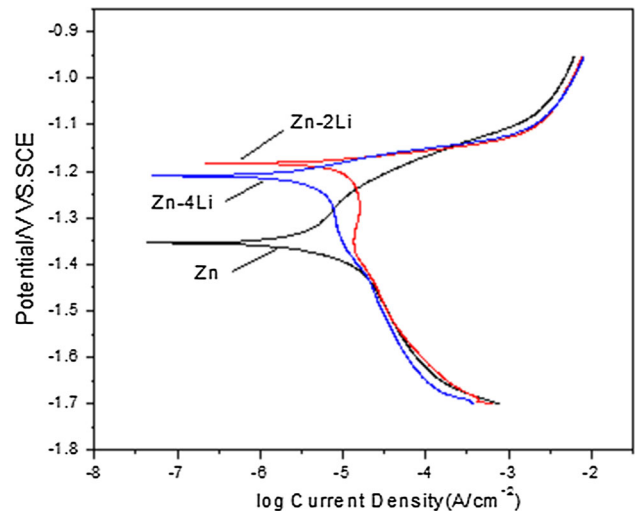


Fig. 8—Potentiodynamic curves of different alloys after immediate immersion in SBF medium.

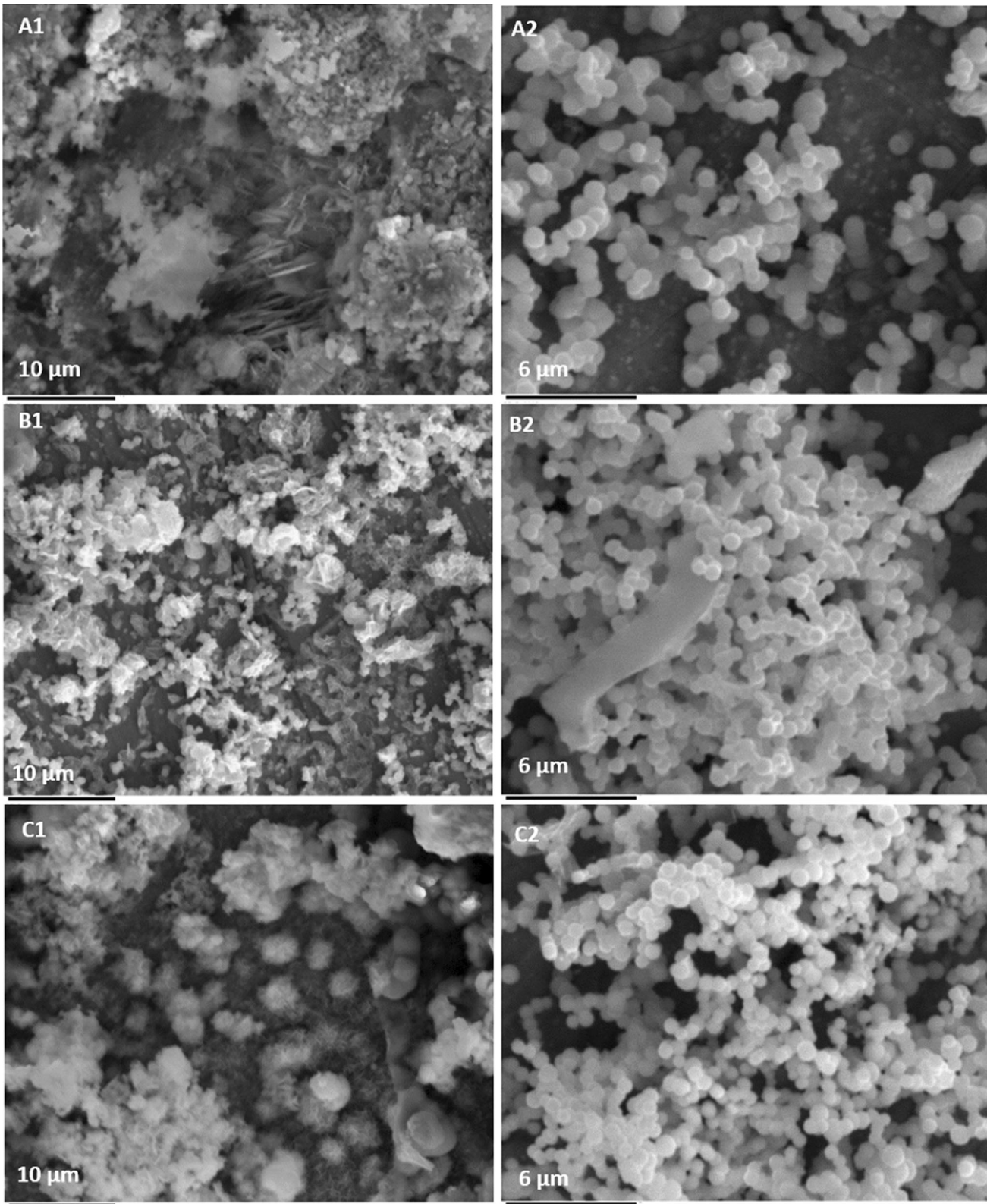


Fig. 9—SEM micrographs of Zn-Li surfaces after immersion in SBF. From row A to C, Li increases from 0 to 2 to 4 at. pct; from column 1 to 2, immersion period increases from 4 to 14 days.

F. Morphology and EDS of Corrosion Products

Images of corroded surfaces are shown in Figure 9 for Zn, Zn-2Li, and Zn-4Li after immersion in SBF for 4

and 14 days. At the 4-day time point, Zn and the two alloys exhibit morphologically different surface deposits. The initial products formed on the Zn substrate

Table VI. Corrosion Potentials, Corrosion Current Densities, and Corrosion Rates Obtained from the Polarization curves, for Zn, Zn-2Li, and Zn-4Li

Sample	E_{corr} (V) vs SCE	i_{corr} ($\mu\text{A}/\text{cm}^{-2}$)	Corrosion Rate (mm/year)
Zn	-1.35	10.96	0.16
Zn-2Li	-1.18	3.98	0.06
Zn-4Li	-1.21	3.80 </tr	

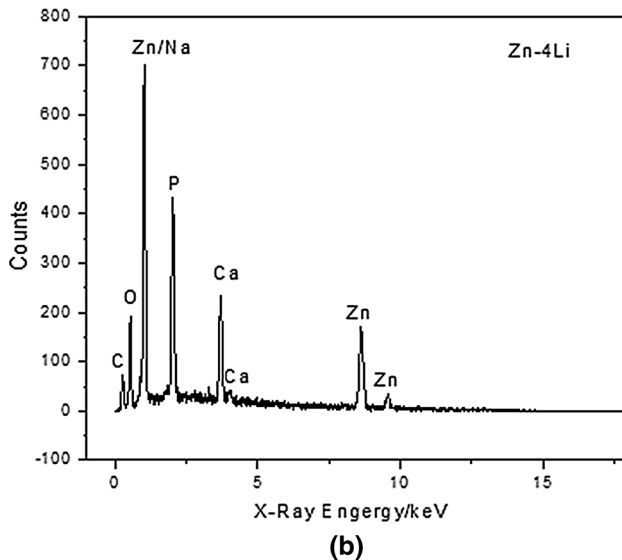
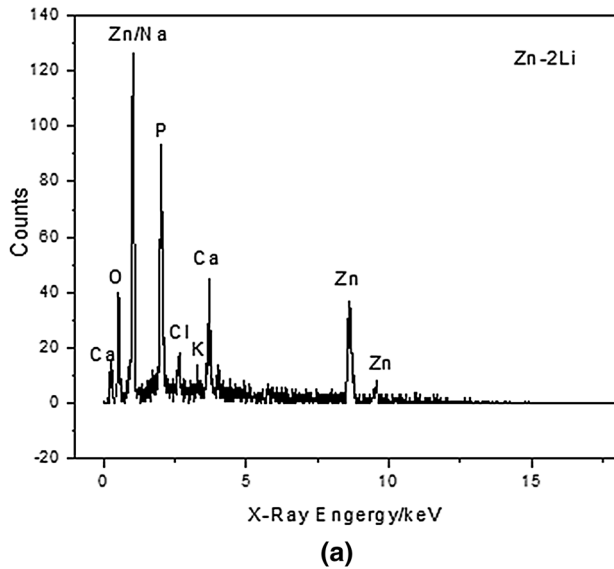


Fig. 10—EDS spectra of Zn-Li alloy surface products after immersion in SBF for 14 days.

comprised sharp elongated crystals, and flower-like and porous aggregates (Figure 9(A1)). The Zn-2Li substrate displays a finer initial crystal network and is decorated with agglomerated clusters on top in light contrast (Figure 9(B1)). The Zn-4Li substrate is covered with

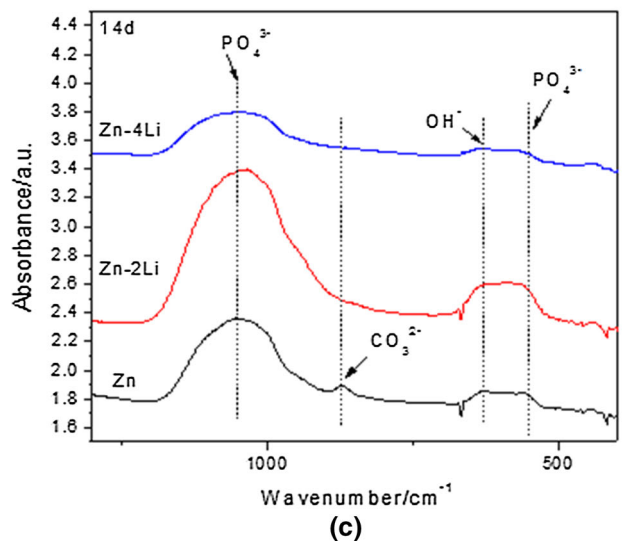
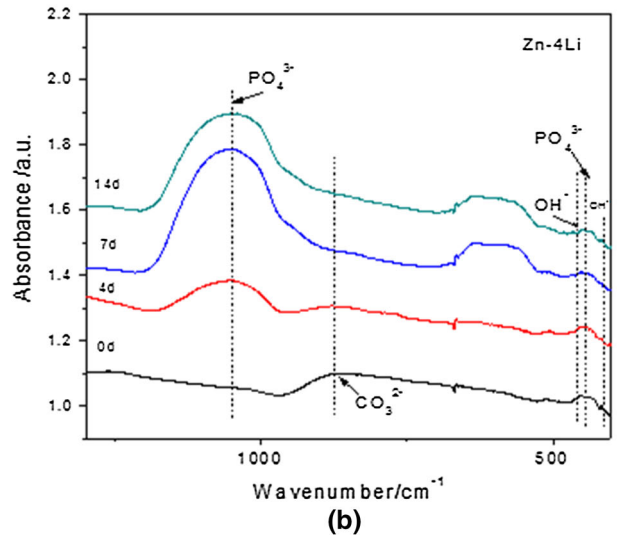
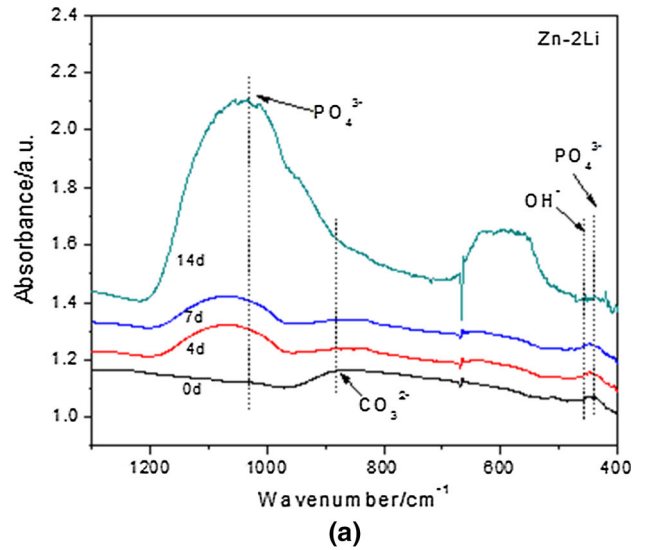


Fig. 11—FTIR spectra after 14-day immersion in SBF for Zn, Zn-2Li, and Zn-4Li.

sponge-like structures embedded with regular spheres and irregular aggregates (Figure 9(C1)). After 14 days of immersion, the three samples appear very similar with each substrate coated in a regular and well-defined population of spherical particles with an average diameter of roughly 1 μm in all cases (Figure 9(A2), (B2), (C2)).

To gain a first approximation of the elemental compositions of the particles formed on the sample surfaces during the immersion testing, EDS analysis of some of the sample surfaces (Figure 10) was performed. These scans confirmed the presence of Ca, P, and O, suggesting that the particles could be mainly composed of calcium phosphate, similar to what was found in a previous study on Mg *in vivo*,^[43] although with a much different morphology.

To determine the phase composition and functional groups among the different alloys after immersion testing, FTIR analysis was employed. In the FTIR spectrum (Figure 11), the PO_4^{3-} group band is observed at 570 cm^{-1} , which is related to asymmetric deformation modes of ν_4 group; the absorption band ranging from 1040 to 1090 cm^{-1} is characteristic of the asymmetrical stretching mode of ν_3 group. The locations of absorption bands for PO_4^{3-} group and OH^- at 631 cm^{-1} , combined with the decrease of Ca^{2+} in SBF medium confirmed through ICP-OES testing, explicitly indicate the formation of hydrated apatite phases in the corroded alloys. Absorption intensity of PO_4^{3-} group and OH^- group (Figure 11(a), (b)) increases with prolonged immersion time, which may indicate improvement of apatite properties making this phase more stable. The presence of CO_3^{2-} bands in pure Zn after 14-day immersion (Figure 11(c)) is identified at 875 cm^{-1} , corresponding to ν_2 stretching mode of CO_3^{2-} . This indicates the possible formation of a calcite phase after immersion, while this peak is missing from both Zn-Li alloys.

IV. CONCLUSIONS

By using a vacuum induction melting technique, a new class of Zn-Li alloys has been cast, hot-rolled, and analyzed for biomedical-focused application. XRD results indicate the formation of LiZn_4 through the emergence of diffraction peaks corresponding to (001) and (004) for this phase when deformed by hot rolling, which increased hardness significantly in all cases. Mechanical testing showed that alloying Zn with Li increases the tensile strength to 360 MPa with a nominal addition of 2 at. pct and 560 MPa with 6 at. pct Li following hot rolling. Addition of Li above the eutectic composition caused a severe decrease in elongation to failure making the 6 pct Li alloy unsuitable for cardiovascular stent application.

Our *in vitro* study with the newly formulated Zn-2Li and Zn-4Li alloys demonstrates that the corrosion rates and products in modified SBF solution closely resemble that of pure Zn observed *in vivo*, in plasma, and in whole blood from the previous studies. The Zn-4Li alloy exhibited higher resistance to corrosion compared to

Zn-2Li suggesting a positive effect of Li content on protective characteristics of the corrosion layer.

ACKNOWLEDGMENTS

U.S. National Institute of Health—National Heart, Lung, and Blood Institute (Grant #1R15HL129199-01) and U.S. National Institute of Health—National Institute of Biomedical Imaging and Bioengineering (Grant #5R21 EB 019118-02) are acknowledged for funding this work. The authors thank Paul Fraley for tensile testing. The authors also thank the staff of the Applied Chemical and Morphological Analysis Laboratory for assisting with the sample preparation for electron imaging.

REFERENCES

1. A. Farb: *Circulation*, 2002, vol. 105, pp. 2974–80.
2. S. Cook, P. Wenaweser, M. Togni, M. Billinger, C. Morger, C. Seiler, R. Vogel, O. Hess, B. Meier, and S. Windecker: *Circulation*, 2007, vol. 115, pp. 2426–34.
3. A. Colombo and E. Karvouni: *Circulation*, 2000, vol. 102, pp. 371–73.
4. P. Erne, M. Schier, and T.J. Resink: *Cardiovasc. Interv. Radiol.*, 2006, vol. 29, pp. 11–16.
5. M. Peuster, P. Wohlsein, M. Brugmann, M. Ehlerding, K. Seidler, C. Fink, H. Brauer, A. Fischer, and G. Hausdorf: *Heart*, 2001, vol. 86, pp. 563–69.
6. R.O.N. Waksman, R. Pakala, R. Baffour, R. Seabron, D. Hellinga, and F.O. Tio: *J. Interv. Cardiol.*, 2008, vol. 21, pp. 15–20.
7. P.K. Bowen, E.R. Shearier, S. Zhao, R.J. Guillery II, F. Zhao, J. Goldman, and J. Drelich: *Adv. Healthc. Mater.*, 2016, vol. 05, pp. 1121–40.
8. S. Nishio, K. Kosuga, K. Igaki, M. Okada, E. Kyo, T. Tsuji, E. Takeuchi, Y. Inuzuka, S. Takeda, T. Hata, Y. Takeuchi, Y. Kawada, T. Harita, J. Seki, S. Akamatsu, S. Hasegawa, N. Bruining, S. Brugaletta, S. de Winter, T. Muramatsu, Y. Onuma, P.W. Serruys, and S. Ikeguchi: *Circulation*, 2012, vol. 125, pp. 2343–53.
9. M. Moravej, F. Prima, M. Fiset, and D. Mantovani: *Acta Biomater.*, 2010, vol. 6, pp. 1726–35.
10. M. Moravej, H. Hermawan, D. Dubé, M. Fiset, and D. Mantovani: *Adv. Mater. Res.*, 2006, vols. 15–17, pp. 113–18.
11. L. Yang and E. Zhang: *Mater. Sci. Eng. C*, 2009, vol. 29, pp. 1691–96.
12. R. Waksman, R. Pakala, P.K. Kuchulakanti, R. Baffour, D. Hellinga, R. Seabron, F.O. Tio, E. Wittchow, S. Hartwig, C. Harder, R. Rohde, B. Heublein, A. Andrae, K.H. Waldmann, and A. Haverich: *Catheter. Cardiovasc. Interv.*, 2006, vol. 68, pp. 607–17.
13. H. Tapiero and K.D. Tew: *Biomed. Pharmacother.*, 2003, vol. 57, pp. 399–411.
14. P.K. Bowen, J. Drelich, and J. Goldman: *Adv. Mater.*, 2013, vol. 25, pp. 2577–82.
15. *Magnesium Technology 2011*, 1st ed., R.J. Werkhoven, and W.H. Sillekens, and J.B.J.M. Lieshoutvan, eds., *Magnesium Technology 2011*, Wiley, New York, 2011, pp. 419–24.
16. D. Vojtech, J. Kubasek, J. Serak, and P. Novak: *Acta Biomater.*, 2011, vol. 7, pp. 3515–22.
17. J.-M. Seitz, M. Durisin, J. Goldman, and J.W. Drelich: *Adv. Health. Mater.*, 2015, vol. 4, pp. 1915–36.
18. X. Zhang, G. Yuan, and Z. Wang: *Mater. Lett.*, 2012, vol. 74, pp. 128–31.
19. F. Kang, J.Q. Liu, J.T. Wang, and X. Zhao: *Adv. Eng. Mater.*, 2010, vol. 12, pp. 730–34.
20. A.D. Pelton: *J. Phase Equilibria*, 1991, vol. 12, pp. 42–45.
21. G.N. Schrauzer: *J. Am. Coll. Nutr.*, 2002, vol. 21, pp. 14–21.

22. Food and Nutrition Board Institute of Medicine, *Washington, DC: National Academy Press* 2001.
23. L. Xu, G. Yu, E. Zhang, F. Pan, and K. Yang: *J. Biomed. Mater. Res., Part A*, 2007, vol. 83A, pp. 703–11.
24. F. Witte, I. Abeln, E. Switzer, V. Kaese, A. Meyer-Lindenberg, and H. Windhagen: *J. Biomed. Mater. Res. A*, 2008, vol. 86, pp. 1041–47.
25. M. Thomann, D. Ch Krause, N. von der Bormann, H. Windhagen. Höh, and A. Meyer-Lindenberg: *Mater. Werkst.*, 2009, vol. 40, pp. 82–87.
26. F. Witte, J. Fischer, J. Nellesen, C. Vogt, J. Vogt, T. Donath, and F. Beckmann: *Acta Biomater.*, 2010, vol. 6, pp. 1792–99.
27. N. von der Höh, A. Krause, D. Bormann, C. Krause, F.-W. Bach, H. Windhagen, and A. Meyer-Lindenberg: *J. Mater. Sci.*, 2010, vol. 45, pp. 624–32.
28. V. Pavlyuk, I. Chumak, L. Akselrud, S. Lidin, and H. Ehrenberg: *Acta Crystallogr. B Struct. Sci. Cryst. Eng. Mater.*, 2014, vol. 70 (Pt 2), pp. 212–17.
29. J. Wang, P. King, and R.A. Huggins: *Solid State Ion.*, 1986, vol. 20, pp. 185–89.
30. Marie.-Pierre. Bichat, Jean.-Louis. Pascal, Frédéric. Gillot, and Frédéric. Favier: *Chem. Mater.*, 2005, vol. 17, pp. 6761–71.
31. E. Zintl, A. Schneider, and Z. Elektrochem: *Angew. Phys. Chem.*, 1935, vol. 41, pp. 764–67.
32. H. Schönemann and H.-U. Schuster: *Rev. Chim. Miner.*, 1976, vol. 13, pp. 32–40.
33. V. Pavlyuk, I. Chumak, and H. Ehrenberg: *Acta Crystallogr. Sect. B*, 2012, vol. 68, pp. 34–39.
34. T. Kokubo, H. Kushitani, S. Sakka, T. Kitsugi, and T. Yamamuro: *J. Biomed. Mater. Res.*, 1990, vol. 24, pp. 721–34.
35. Standard Practice for Laboratory Immersion Corrosion Testing of Metals ASTM G31-72, (ASTM International: West Conshohocken, PA, 2004).
36. Q. Wang, L.L. Tan, W.L. Xu, B.C. Zhang, and K. Yang: *Mater. Sci. Eng. B*, 2011, vol. 176, pp. 1718–26.
37. F. Witte, J. Fischer, J. Nellesen, H.A. Crostack, V. Kaese, A. Pisch, F. Beckmann, and H. Windhagen: *Biomaterials*, 2006, vol. 27, pp. 1013–18.
38. L. Yang and E.L. Zhang: *Mater. Sci. Eng. C*, 2009, vol. 29, pp. 1691–96.
39. J. A. Helson and H. J. Brems: *Metals as Biomaterials*. Wiley, New York, 1998, pp 101–51.
40. M.A. Khan, R.L. Williams, and D.F. Williams: *Biomaterials.*, 1999, vol. 20, pp. 631–37.
41. J.L. Pascal, M.P. Bichat, F. Gillot, and F. Favier: *Chem. Mater.*, 2005, vol. 17, pp. 6761–71.
42. Denny A. Jones, *Principles and prevention of corrosion (2nd Edition)* 1996.
43. P.K. Bowen, J. Drelich, and J. Goldman: *Acta Biomater.*, 2014, vol. 10, pp. 1475–83.